**Supporting Information**

# Ultrathin Tin Monosulfide Nanosheets with Exposed (001) Plane for Efficient Electrocatalytic Conversion of $CO_2$ into Formate

Hanlin Chen,[+,a] Junxiang Chen,[+,c] Jincheng Si,[a] Yang Hou,*[,a,f] Qiang Zheng,[e] Bin Yang,[a] Zhongjian Li,[a] Liguo Gao,[b] Lecheng Lei,[a] Zhenhai Wen,*[,c] Xinliang Feng*[,d]

[a] Key Laboratory of Biomass Chemical Engineering of Ministry of Education, College of Chemical and Biological Engineering, Zhejiang University, Hangzhou, 310027, China

[b] State Key Laboratory of Fine Chemicals, School Petroleum and Chemical Engineering, Dalian University of Technology, Panjin, 124221, China

[c] CAS Key Laboratory of Design and Assembly of Functional Nanostructures, Fujian Provincial Key Laboratory of Nanomaterials, Fujian Institute of Research on the Structure of Matter, Chinese Academy of Sciences, Fuzhou, 350002, China

[d] Center for Advancing Electronics Dresden (cfaed) and Department of Chemistry and Food Chemistry, Technische Universität Dresden, Mommsenstraße 4, 01062 Dresden, Germany

[e] Correlated Quantum Materials Group, Materials Science and Technology , Division Oak Ridge National Laboratory, 1 Bethel Valley Road Oak Ridge, TN37831, USA

[f] Ningbo Research Institute, Zhejiang University, Ningbo 315100, China

**Synthesis of bulk SnS**

The bulk SnS was synthesized by a solid-state synthesis method. Typically, S powder and Sn power with a stoichiometric proportion were sealed in a vacuum quartz tube and heated at 500 $^{o}$C for 24 h, and the obtained product was used as bulk SnS.

**Synthesis of SnS NSs**

A commercial Cu tape was used as host or current collector of the bulk SnS. The Pt plate (1 x 1 $cm^2$) electrode and bulk SnS electrode were applied as counter electrode and working electrode in a homemade cell with 0.5 M $Na_2SO_4$ solution as electrolyte. The two electrodes were parallel with each other with a distance of 2.0 cm. An initial negative DC voltage of 2.0 V was applied on bulk SnS electrode for 3 min. Afterwards, the negative DC voltage was slowly increased to 5.0 V and maintained this voltage for 5 min. Further, the voltage was alternated to the positive voltage of 3.0 V and maintained 30 s. The cathodic and anodic processes were carried out about 15 times to accumulate enough exfoliated SnS. All the exfoliation process was carried out at near-constant temperature of 15 $^{o}$C to avoid overheat. The exfoliated SnS was cleaned by 0.5 M $H_2SO_4$ and washed with enough deionized water to remove electrolytes. The exfoliated SnS was dispersed in DMF solution and sonicated in cell crushing machine. The supernatant liquid was collected with next 3,500 rpm centrifugation for 30 min, followed by 10,000 rpm centrifugation. The final product of SnS NSs was collected from the bottom of centrifuge tube after lyophilizing treatment.

**Synthesis of SnS NSs electrode via particle transfer method**

The SnS NSs electrode was fabricated by using a particle transfer method (Chem. Sci., 2013, 4, 1120). The SnS NSs was first dispersed in isopropanol, and then drop-casting onto a glass substrate. A Ti layer was tiled onto the SnS NSs layer by electronic beam evaporation method. The layers of Ti/SnS NSs were stuck to another glass substrate, and then peeled off the former glass substrate. An ultrasonication treatment was used to remove the superfluous SnS NSs, and then the SnS NSs electrode (SnS NSs/Ti/glass) was fabricated. A Cu wire was connected onto the contacting and conducting layers using In solder. The redundant part was thoroughly

covered with an epoxy resin (Chem. Commun., 2017, 53, 629).

**Characterization**

XPS spectra were recorded by an X-ray photoelectron spectroscopy (Escalab 250Xi) using radiation of Al Ka. The FESEM images were taken from a field emission SEM (Supra 55). The HRTEM images were performed on a high-resolution with 200 kV TEM (JEM-2100). XRD data were obtained from a RIGAKU D/MAX 2550/PC device with radiation of the Cu Kα. Raman results were recorded with 532 nm wavelength (LabRAM HR Evolution). AFM images were performance with tapping Mode (MultiMode VEECO). The F.E. of liquid and gas productions were measured on nuclear magnetic resonance (BRUKER AVIII500M) and gas chromatography (9790 II). The SnS NSs was sonicated in acetone for 20 min. After that, drops of the resulting suspensions were deposited on lacey carbon copper grids, and then dried in air for STEM. High-angle annular dark-field-STEM (HAADF-STEM) was performed on an aberration-corrected Nion UltraSTEM 100TM, equipped with a cold field emission electron source and a corrector of third and fifth order aberrations, operated at an accelerating voltage of 100 kV. The convergence semi-angle of the incident probe was 30 mrad, and the HAADF images were collected with semi-angle of 86-200 mrad. The HAADF images were also simulated using QSTEM program package. XANES and EXAFS analysis were performed in Beijing Synchrotron Radiation Facility (BSRF, Beijing, China) and Shanghai Synchrotron Radiation Facility.

**Electrochemical measurements**

Electrochemical measurements were carried on the electrochemical workstation (CHI 760E). The $CO_2$RR process was performed in 0.5 M $KHCO_3$ solution by a conventional double-pool electrolytic cell with a standard three-electrode system at room temperature. The SnS NSs was dropped on the carbon paper with a loading amount of 1.0 mg $cm^{-2}$. The Ag/AgCl electrode was used as reference electrode. Linear sweep voltammetry (LSV) curves were performed at a scan rate of 5 mV $s^{-1}$. Before LSV measurements, cyclic voltammetry (CV) curves with a scan rate of 50 mV $s^{-1}$ were carried out to activate the working electrode. Electrochemical impedance spectroscopy was performed from 0.01 Hz to 100 kHz at -1.4 V. Electrochemical

surface area (ECSA) was measured at different scan rates of 120, 100, 80, 60, 40, and 20 mV $s^{-1}$ with the potential scale of 0.1 V - 0.2 V.

**Mechanism analysis of electrochemical exfoliation process**

The ions insertion and gas generation are proposed to illustrate the exfoliation mechanism. Under the bias voltage of 5.0 V, the anode triggers countless $H^+$ and $O^{\bullet}$.[1] The $H^+$ is proposed to migrate and gather on the surface of SnS interplanar. The reduction of $H^+$ could generate $H_2$ bubbles, which induces a great force between the SnS layers and exfoliates the neighbor layers. At the same time, the $Na^+$ ions with diameter of 0.12 nm are also supposed to insert into SnS cathode freely.[2] Although the small diameter of $Na^+$ ions could not contribute to the expansion of SnS interlayers, the HER process on the SnS cathode can occur and take a key step for electrochemical exfoliation. The cathodic process results in a low-efficiency exfoliation, and accelerates the intercalation of $SO_4^{2-}$ ions.

$$H_2O \rightarrow HO^{\bullet} + 2H^+ + 2e^- \rightarrow 2H^+ + O^{\bullet} + 2e^- \quad (S1)$$

$$2H^+ + 2e^- \rightarrow H_2 \quad (S2)$$

Unlike the $Na^+$ ions, the $SO_4^{2-}$ ions present a large diameter of 0.46 nm, and even greater than interplanar of SnS (0.39 nm). When altering to the positive voltage, the $SO_4^{2-}$ ions migrates and inserts into the enlarged interplanar of bulk SnS, which further expands the distance of SnS interplanar. Meanwhile, the radicals ($HO^{\bullet}$, $O^{\bullet}$) produced on anode attack the boundaries or intrinsic defects in SnS, thus resulting in the opening edges. When the positive voltage is altered to negative voltage, the intercalated $SO_4^{2-}$ ions will be reduced into $SO_2$ bubbles.[3] Once the cathodic process and anodic process are completed, the SnS interplanar is expanded to a large extent, and the electrochemical reactions between the interface of SnS layers and electrolyte could generate a lot of gaseous species (e.g., $H_2$, $O_2$, $SO_2$), which are crucial for the electrochemical exfoliation of bulk SnS. Among the electrochemical exfoliation process, the alternate voltage presents significantly improved exfoliation efficiency.

$$2H_2O \rightarrow O_2 + 4H^+ + 4e^- \quad (S3)$$

$$2H_2O + 4e^- \rightarrow H_2 + 2OH^- \quad (S4)$$

$$2SO_4^{2-} + 4H^+ + 2e^- \rightarrow 2H_2O + 2SO_2 \quad (S5)$$

**Computational hydrogen electrode (CHE) method.**

Generally speaking, when studying about the electrocatalytic reaction through first principle, there are two difficulties, one is to calculate the reaction barrier of the proton coupled electron transfer (PCET) reaction; the another one is the Gibbs free energy of the solvated $H^+$. The CHE method proposed by Nørskov *et al*, which can well address these two difficulties, was used in this study. In the framework of CHE method,

$H^+ + e \rightarrow 1/2H_2$ (S6)

the reaction (6) reaches equilibrium on $U_{SHE} = 0$ V, one can replace the energy of $H^+$ with that of $1/2H_2$:

$G_{H+}=1/2GH_2$ (S7)

The energy of electron can be expressed by $-Ue$, where $U$ is the electrode potential *vs.* SHE. As for the reaction barrier of PCET, the CHE method assumes that the overpotential of the electrocatalytic reaction is the overpotential least to make standard reaction Gibbs free energies of all elementary steps to be exothermic. Such potential is called as reaction limiting potential, which is denoted as $U_l$. Usually, $U_l$ is an activity descriptor, as for $CO_2$RR, $U_l$ can be used to judge the exact reaction pathway.

**Reaction models and pathways.**

Similar to our previous work, the "pin model" is used to confirm the reactive site. With the affinity diagram of adsorbates CO* given in Figure S10. We hence find the active site, which provides the strongest bonding locates on the surface Sn for both SnS100 and SnS002.

As for the pathway, the reaction mechanisms for $CO_2$RR to produce HCOOH (l) can be described as below:

$CO_2 + H^+ + e^- + * \rightarrow COOH*$ (RS1)

$COOH* + H^+ + e \rightarrow HCOOH\ (l)$ (RS2)

The total reaction is $CO_2$ (g) + $2H^+$ + 2e → HCOOH (l) and its equilibrium potent is -0.20 + 0.059 (pH-4). The associated pH in this work is 7.2, which gives the equilibrium potential to be -0.0112 V. This is very close to the equilibrium of hydrogen electrode reaction (0 V). This is the reason we see a similar free energy of the production of HER and HCOOH (l) in the FED of Figure 5. Besides (RS2), the protonation of COOH* is also possible to generate CO (g), by

$COOH^* + H^+ + e \rightarrow CO^* + H_2O$ (l) (RS2)

$CO^* \rightarrow CO$ (g) (RS3)

With a total reaction written as $CO_2$ (g) + $2H^+$ + 2e → CO (g) + $H_2O$ (l), the equilibrium potential is -0.1 V. As for HER, despite the HER process could follow Heyrovsky-Volmer or Tafel-Volmer pathway, they are undistinguishable in Nørskov's approach. Thus, the Volmer- Heyrovsky mechanism was given here:

$H^+ + e^- + * \rightarrow H^*$ (RS4)

$H^* + H^+ + e^- \rightarrow * + H_2$ (RS5)

The equilibrium potentials of -0.0112, 0, and -0.1 V are used to calculate the free energies of HCOOH (l), CO (g), and $H_2$ (g) from the free energy of $CO_2$ (g) in order to avoid the error for DFT calculation.

**DFT details**

Spin polarized DFT calculations with DMol3 module[21] in the Materials Studio program of Bio Accelrys were performed in this work. The generalized gradient approximation (GGA) method with Perdew-Burke-Ernzerhof (PBE)[22] was used to describe the exchange correlation functional component of the Hamiltonian. All electrons were adopted as Core treatment without using pseudo potential. The double numerical plus polarization function basis set was used. The method of dispersion correction was acted as an add-on to standard Kohn–Sham density functional theory (DFT-D). A smearing of 0.005 Ha to the orbital occupation and $1 \times 10^{-6}$ Ha convergence criterion for self-consistent-field (SCF) calculations were applied. The

geometry optimization convergence tolerance for energy change, max force, and max displacement were $1 \times 10^{-5}$ Ha, 0.002 Ha/Å, and 0.005 Å, respectively. We performed the geometry optimization for SnS unit cell, which gave an 11.42 Å of lattice parameter. All the atoms allowed relaxing during the optimization. In calculating the Gibbs free energy differences from (RS1) to (RS5), the associated adsorption free energy of the adsorbates was calculated by the following expression:

$$G_A = E_A + ZPE - TS + \int C_p dT \quad \text{(S8)}$$

where $E_A$ is the total energy of a certain molecule or adsorbate A*. When A is representing a certain molecule, the total energies can be calculated directly. When A is representing a certain adsorbate, it is calculated by the difference between the DFT based substrate with ($E_{A*}^{DFT}$) and without adsorbate A ($E_{*}^{DFT}$):

$$E_A = E_{A*}^{DFT} - E_{*}^{DFT} \quad \text{(S9)}$$

*ZPE*, *TS,* and $\int C_p dT$ are the corrections from zero point energy, entropy, and heat capacity, whose values are listed on Table S2. Other than that, the $H^+$ is calculated by the Gibbs free energy of $1/2H_2$; the energy of electron is calculated by -Ue. As for the solvation energies, a value of -0.11 eV is added to each O atom of adsorbates. For instance, -0.11 eV and -0.22 eV are added for OH* and COOH*. Such correction can lead an agreement with experimental overall half reaction of $CO_2$ reduction.

**The origin of the improved activity of defect sites**

Both for SnS100 and SnS001, the defect sites possess the higher activities than the intact sites. It may be an interesting issue to figure out the intrinsic reason. Figure S11 depicts a projected density of state (PDOS) analysis of the reactive site (Sn marked by orange) with and without S defect. The generating of S defect both cause the negative shift of the Sn PDOS orbitals. Driven by this, the anti-bonding orbital of Sn is shifted bellow the Fermi Energy ($E_f$), and then is filled by electrons. The filling of anti-bonding orbital will cause the weakening of bonds between tin and its surrounding S, thus resulting in a generation of new orbitals to bond with the adsorbates. Consistently, we can see a much larger PDOS of Sn around $E_f$ for defect site

compared with the intact site, both for SnS100 and SnS001. This higher reactivity for defect site is the exact reaction for a better activity of defect site than the bulk site.

**Figure S1.** Mass production of SnS NSs.

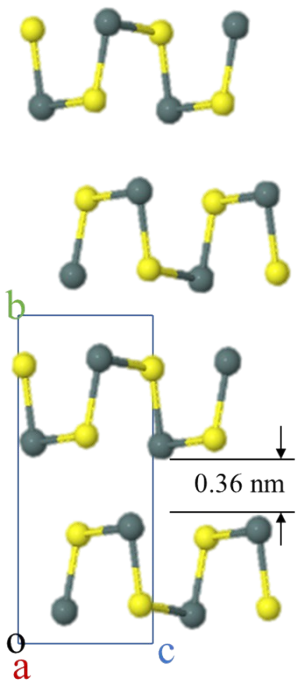


**Figure S2.** Crystal structure of SnS. As-synthesized bulk SnS has an orthorhombic structure with space group Pbnm 62 (a = 4.32 Å, b = 11.19Å, c = 3.98 Å). The SnS layer was tightly stacked along b-cis with an interlayer distance of 0.36 nm.

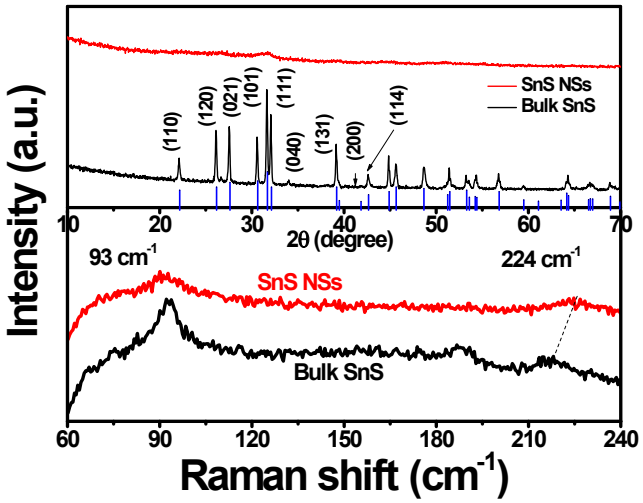


**Figure S3.** Raman spectra and XRD patterns of bulk SnS and SnS NSs.

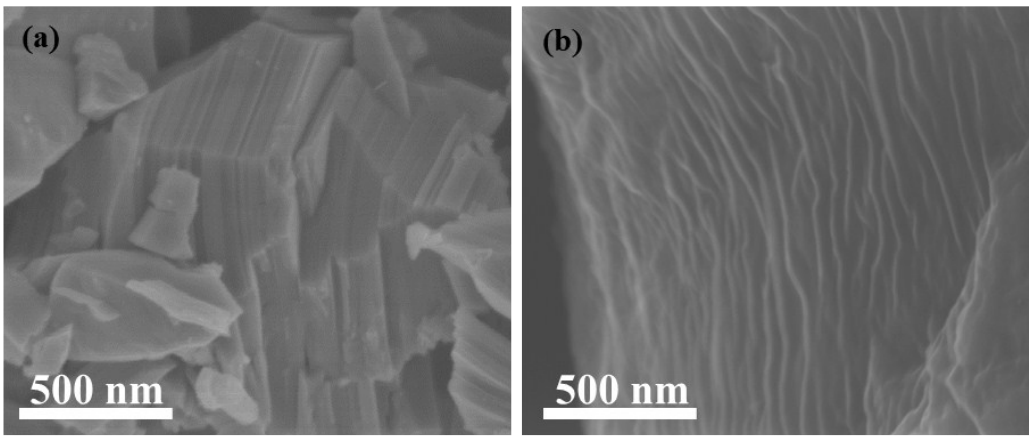


**Figure S4.** FESEM images of bulk SnS (a) and exfoliated SnS (b).

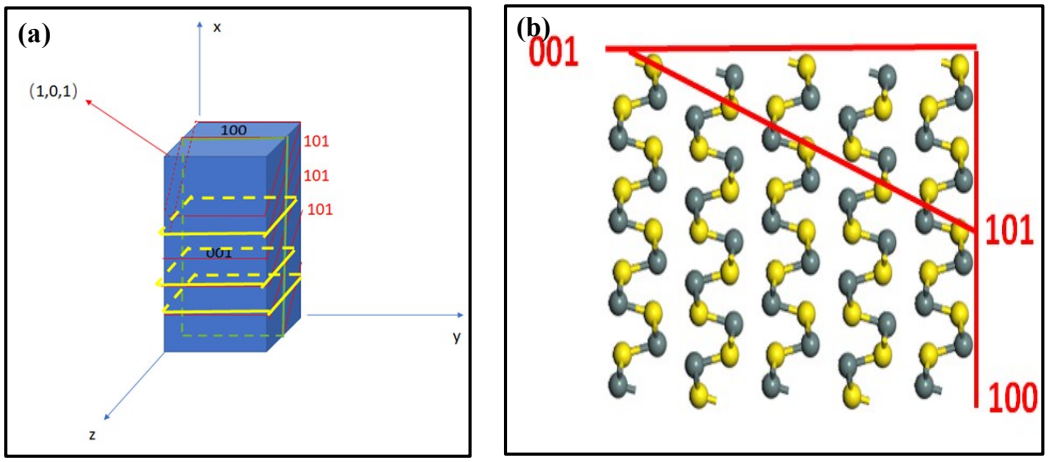


**Figure S5.** (a) Schematic planes information of SnS, and (b) relative location of SnS planes.

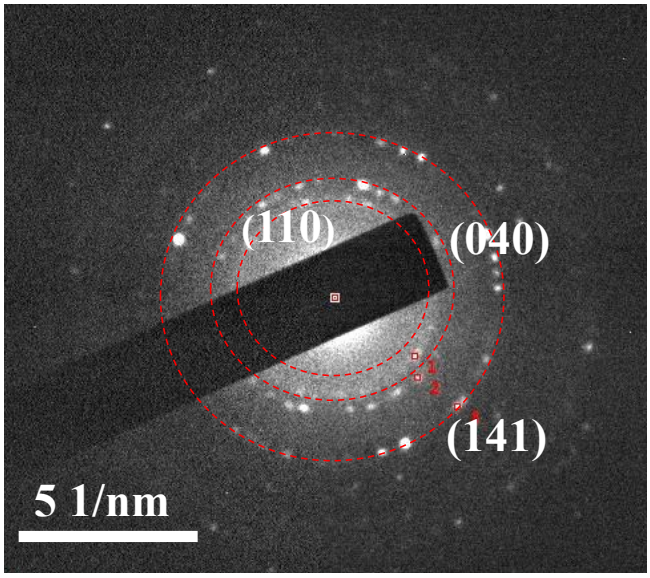


**Figure S6.** SAED pattern of SnS NSs.

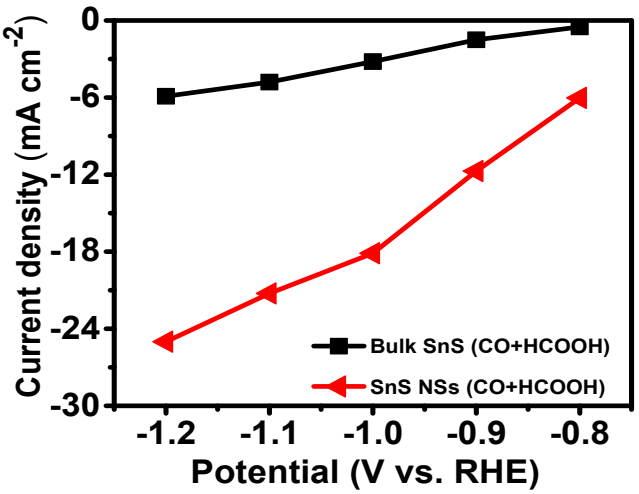


**Figure S7.** Partial current densities (C1 products) of $CO_2$RR for bulk SnS and SnS NSs.

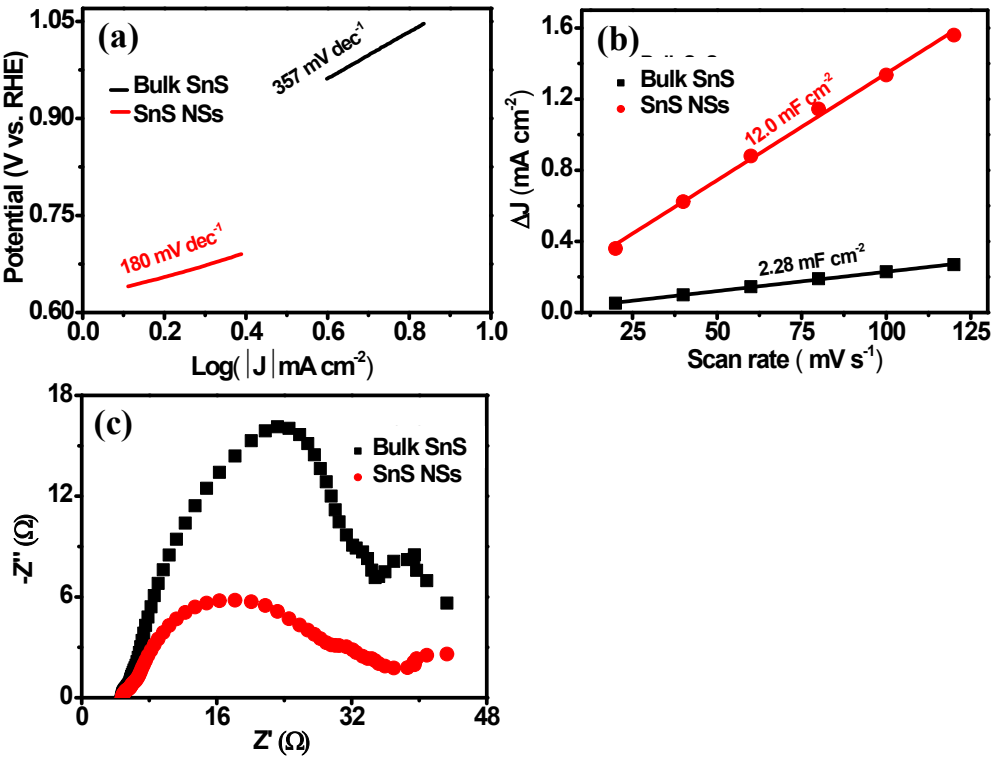


**Figure S8.** (a) Tafel plots, (b) ECSA, and (c) EIS spectra of bulk SnS and SnS NSs.

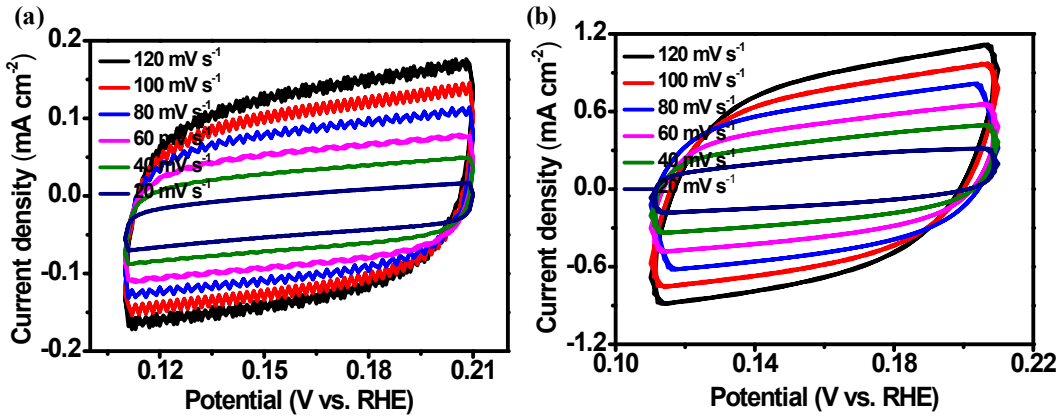


**Figure S9.** CV curves of (a) bulk SnS and (b) SnS NSs.

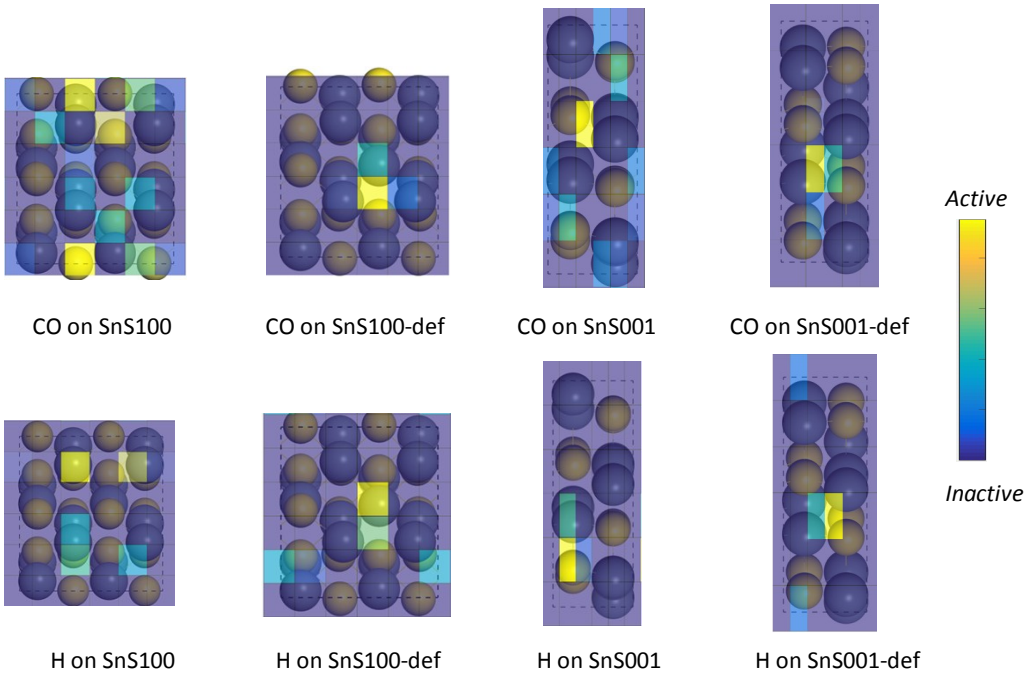


**Figure S10.** The result of "pin model" to probe the active site on the surface for DFT calculations. Each surface has been divided into 5 x 5 girds. The adsorbates H and CO are placed in each grid and relaxed only in the normal of the surface. The adsorption energies calculated in these ways are plotted by colors, where a site with the brighter color indicates a stronger adsorption. Four kinds of sites mentioned in this work, and their interaction towards adsorbates CO* and H* are studied. In addition, we consider that the COOH* shares the same active sites with CO*.

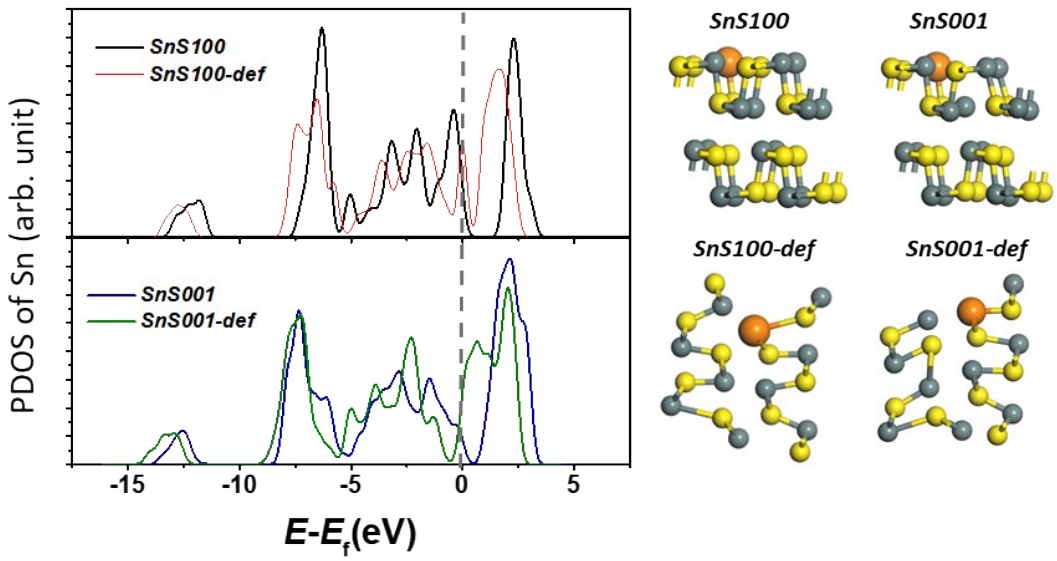


**Figure S11.** (Left) The PDOS of the reactive Sn in SnS100 (blank), SnS100-def (red), SnS001 (blue), and SnS001-def (green). (Right) The positions of the associated reactive Sn that is colored by orange.

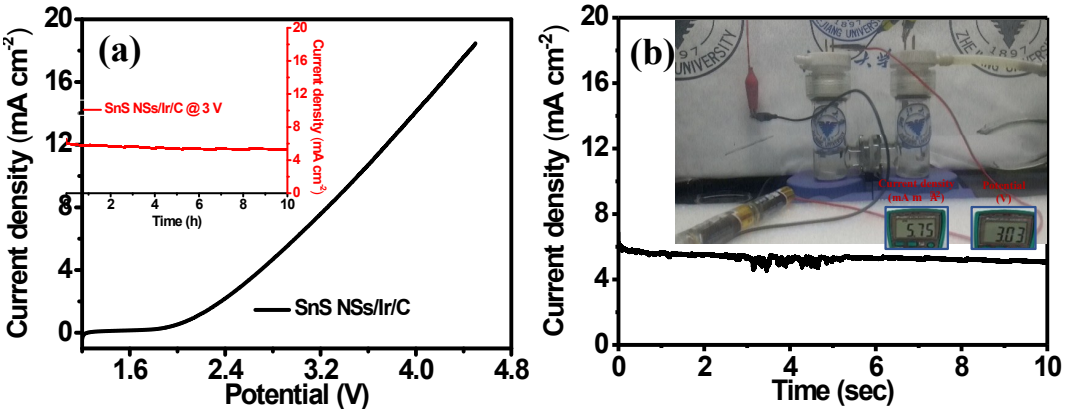


**Figure S12. (a)** Polarization curve of SnS NSs/Ir/C couple in two-electrode system. Inset: current density of SnS NSs/Ir/C couple at 3.0 V. (b) Chronoamperometry measurement of SnS NSs/Ir/C couple driven with two 1.5 V AA batteries. Inset: digital image of two-electrode device for SnS NSs/Ir/C couple.

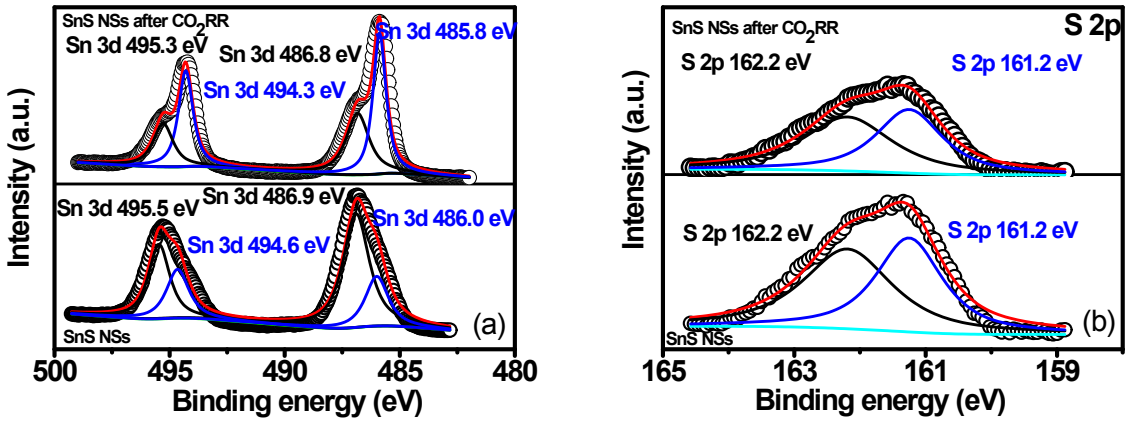


**Figure S13.** High resolution Sn 3d (a) and S 2p (b) XPS spectra for SnS NSs before and after $CO_2$RR tests (2 h).

The high resolution Sn 3d XPS spectra exhibited a relative strong $Sn^{2+}$ peak for SnS NSs after $CO_2$RR catalysis (Figure S13a), indicating that the SnS NSs remained a stable structure after long-time $CO_2$RR reaction. Actually, after $CO_2$RR catalysis, the SnS NSs displayed a slight red shift for the max absorption position (white line) as compared with SnS NSs before $CO_2$RR, indicating that the SnS NSs has a lower oxidation (Figure 4f). Moreover, except the $Sn^{2+}$-O bonds (oxidation under air atmosphere) at 1.44 Å for SnS NSs and bulk SnS, after $CO_2$RR test, the main peak located at 2.11 Å ($Sn^{2+}$-S) for SnS NSs also demonstrated that the Sn in the SnS NSs remained the initial $Sn^{2+}$, which is consistent well with the XPS results. In addition, after $CO_2$RR electrocatalysis, the high resolution S 2p XPS spectra of SnS NSs demonstrated no obvious change compared with that of pristine SnS NSs (Figure S13b), implying that the prepared SnS NSs had good stability.

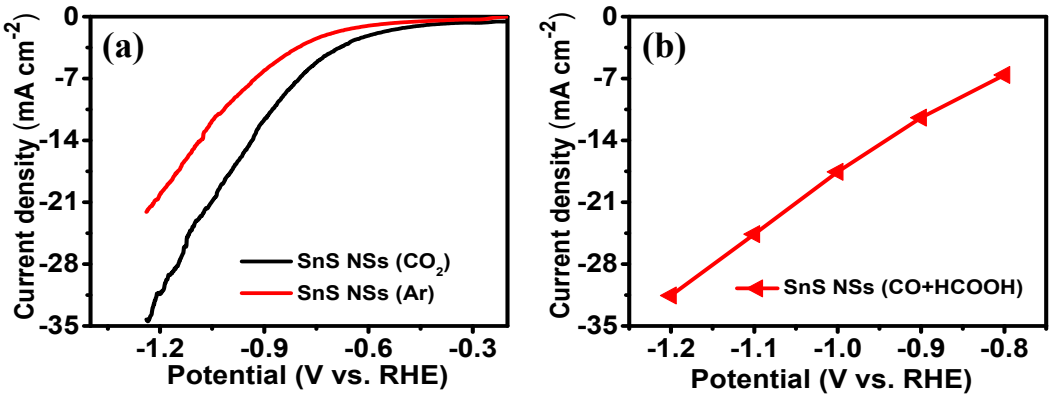


**Figure S14.** (a) Polarization curves of SnS NSs electrode prepared via a particle transfer method in Ar-saturated and $CO_2$-saturated electrolytes. (b) Partial current density of SnS NSs electrode prepared via a particle transfer method for HCOOH and CO productions.

**Table S1.** HCOOH F.E. of recent other reported Sn-based $CO_2$RR electrocatalysts.

| Sample | Electrolyte | F.E. | Partial current density (mA $cm^{-2}$) | Potential (V) to achieve partial current density | Reference |
|---|---|---|---|---|---|
| **SnS NSs** | **0.5 M $KHCO_3$** | **82.1%** | **18.9** | **-1.1** | **This work** |
| **SnS NSs prepared by particle transfer method** | **0.5 M $KHCO_3$** | **91%** | **22.3** | **-1.1** | **This work** |
| $SnS_2$/Sn on rGO | 0.5 M $NaHCO_3$ | 84.5% | 11.7 | -1.4 | Nano Energy, 2017, 31, 270 |
| Ni doping $SnS_2$ nanosheets | 0.5 M $KHCO_3$ | 93% | 19.6 | -0.9 | Angew. Chem. Int. Ed., 2018, 57, 10954 |
| $SnS_2$ nanosheets | 0.5 M $KHCO_3$ | 50% | 6.2 | -0.9 | Angew. Chem. Int. Ed., 2018, 57, 10954 |
| $SnS_2$ monolayer | 0.1 M $KHCO_3$ | 94 ± 5% | 45.2 | -0.8 | J. Catal., 2018, 364, 125 |
| Bulk $SnS_2$ | 0.1 M $KHCO_3$ | 29 ± 3% | 1.1 | -0.8 | J. Catal., 2018, 364, 125 |
| Sn(S)/Au | 0.1 M $KHCO_3$ | 93% | 55.0 | -0.75 | Joule, 2017, 1, 794 |
| Ag-$SnS_2$ nanosheets | 0.5 M $NaHCO_3$ | 65.5% | 22.5 | -0.9 | Small, 2019, 1904882 |
| $SnS_2$ nanosheets | 0.5 M $NaHCO_3$ | 56.2% | 15.1 | -0.9 | Small, 2019, 1904882 |
| Bulk $SnS_2$ | 0.5 M $NaHCO_3$ | 55.6% | 9.2 | -0.9 | Small, 2019, 1904882 |

| | | | | | |
|---|---|---|---|---|---|
| Cu-S co-doped $SnO_2$ | 0.5 M $NaHCO_3$ | 58.5% | N/A | N/A | ChemElectroChem, 2018, 5, 1330 |
| Electrodeposited $Sn/SnO_2$ | 0.5 M $NaHCO_3$ | ~40% | 32.0 | -0.7 | J. Am. Chem. Soc., 2012, 134, 1986 |
| $SnO_2$-CuO | 0.5 M $KHCO_3$ | 50% | N/A | N/A | Catal. Today, 2018, 318, 2 |
| 1D $SnO_2$ | 0.1 M $KHCO_3$ | 70% | 7.0 | -1.29 | Adv. Funct. Mater., 2018, 28, 1706289 |
| Partial oxide Sn | 0.1 M $KHCO_3$ | 70% | N/A | N/A | ACS Catal, 2016, 6, 7824 |
| Mesoporous $SnO_2$ | 0.1 M $KHCO_3$ | 75% | 10.8 | -1.15 | ACS Sustainable Chem. Eng., 2018, 6, 1670 |
| Sn quantum sheets/GO | 0.1 M $KHCO_3$ | 60% | N/A | N/A | Nat. Commun., 2016, 7, 12697 |
| Sn gas diffusion electrode | 0.5 M $KHCO_3$ | 73% | 17.4 | -1.8 | J. Power Sources, 2014, 271, 278 |

**Table S2.** The correction from the zero point energy, entropy and heat capacity for converting the total energies to Gibbs free energies (units: eV).

| Species | ZPE | TS | $\int C_p dT$ |
|---|---|---|---|
| COOH* | 0.63 | 0.17 | 0.09 |
| CO* | 0.22 | 0.08 | 0.05 |
| H* | 0.17 | 0.007 | 0.005 |

**Reference**


1. X. M. Feng, X. Wang, W. Cai, S. L. Qiu, Y. Hu and K. M. Liew, *Acs Applied Materials & Interfaces*, 2016, **8**, 25552-25562.
2. S. Yang, K. Zhang, A. G. Ricciardulli, P. Zhang, Z. Liao, M. R. Lohe, E. Zschech, P. W. M. Blom, W. Pisula, K. Müllen and X. Feng, *Angewandte Chemie*, 2018, **130**, 4767-4771.
3. S. Yang, A. G. Ricciardulli, S. Liu, R. Dong, M. R. Lohe, A. Becker, M. A. Squillaci, P. Samori, K. Mullen and X. Feng, *Angew Chem Int Ed Engl*, 2017, **56**, 6669-6675.